

Toward Efficient Carbon Nanotube/P3HT Solar Cells: Active Layer Morphology, Electrical, and Optical Properties

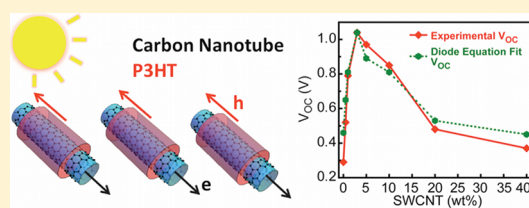
Shenqiang Ren,^{†,§} Marco Bernardi,^{†,§} Richard R. Lunt,[‡] Vladimir Bulovic,[‡] Jeffrey C. Grossman,^{*,†} and Silvija Gradečak^{*,†}

[†]Department of Materials Science and Engineering and [‡]Department of Electrical Engineering and Computer Science, Massachusetts Institute of Technology, Cambridge, Massachusetts 02139, United States

S Supporting Information

ABSTRACT: We demonstrate single-walled carbon nanotube (SWCNT)/P3HT polymer bulk heterojunction solar cells with an AM1.5 efficiency of 0.72%, significantly higher than previously reported (0.05%). A key step in achieving high efficiency is the utilization of semiconducting SWCNTs coated with an ordered P3HT layer to enhance the charge separation and transport in the device active layer. Electrical characteristics of devices with SWCNT concentrations up to 40 wt % were measured and are shown to be strongly dependent on the SWCNT loading. A maximum open circuit voltage was measured for SWCNT concentration of 3 wt % with a value of 1.04 V, higher than expected based on the interface band alignment. Modeling of the open-circuit voltage suggests that despite the large carrier mobility in SWCNTs device power conversion efficiency is governed by carrier recombination. Optical characterization shows that only SWCNT with diameter of 1.3–1.4 nm can contribute to the photocurrent with internal quantum efficiency up to 26%. Our results advance the fundamental understanding and improve the design of efficient polymer/SWCNTs solar cells.

KEYWORDS: Carbon nanotube, P3HT, organic photovoltaics, open-circuit voltage, dark saturation current



Single-walled carbon nanotubes (SWCNTs) are attractive nanomaterials for the development of organic solar cells due to their high carrier mobility, intrinsic one-dimensionality, and tunable optical and electronic properties.¹ The success of bulk heterojunction (BHJ) solar cells based on the fullerene derivative PCBM² has encouraged numerous attempts to replace fullerenes with SWCNTs as electron acceptors with the aim of improving the transport in the polymer blend and the overall device efficiency. BHJ solar cells using conjugated polymers as donors and SWCNTs as acceptors have been reported by several groups,^{3–6} but increasing their power conversion efficiency has proven challenging; three key factors affecting the device performance are the nanotubes electronic structure, their diameter, and the morphology of the active layer, as discussed below.

Semiconducting SWCNTs (s-SWCNTs) display type-II alignment and ultrafast charge transfer with conjugated polymers such as P3HT,^{7–10} and it has been suggested that they can act as efficient acceptors at the interface with P3HT.^{4,8} By contrast, recent investigations showed that metallic SWCNTs (m-SWCNTs) in the active layer have detrimental impact on the photocurrent,⁷ and theoretical studies have predicted that the band alignment of P3HT/m-SWCNTs is unfavorable for charge separation.⁸ So far, most reported BHJ polymer/SWCNTs solar cells have been based on a typical mixture of nonenriched two-thirds semiconducting and one-third metallic SWCNTs^{3–6} and have shown significantly lower efficiencies than fullerene-based devices. For example, P3OT/SWCNTs BHJ cells reported by Kymakis et al. showed a record AM1.5 power conversion efficiency of 0.05%.³

Their work suggested that metallic nanotubes are responsible for a large drop in the device efficiency at relatively low SWCNT concentration (2 wt %) with an optimal nanotube loading of ~1 wt %.⁴

The SWCNT diameter (d) crucially influences the nanotube optical properties, as well as the charge and exciton transport in the active layer. The use of s-SWCNT of larger diameter would be advantageous due to their lower exciton binding energy that scales as $\sim 1/d^{11}$ and because of the larger carrier mobility in the diffusive transport regime that scales as d^2 .¹² On the other hand, small-diameter tubes ($d < 1$ nm) are predicted to have larger band offsets and thus more efficient exciton dissociation.¹⁰ A trade-off between these two aspects is expected to yield optimal results at intermediate nanotube diameters (e.g., $1.3 \text{ nm} < d < 1.5 \text{ nm}$).

Finally, optimization of the active layer morphology is required for the prevention of nanotube bundling, defined here as the formation of μm -scale aggregates of nanotubes. SWCNT aggregation reduces the amount of interface available for charge separation, alters the properties of the isolated tubes, and allows only for low concentrations of SWCNTs to be achieved. However, the study of the electrical and optical properties of P3HT/SWCNTs devices with the aim of understanding different regimes for exciton and charge carrier dynamics requires use of a wide range of nanotube concentrations.

To address these device performance factors, in this Letter we investigate P3HT/SWCNTs solar cells by utilizing high-purity

Received: August 12, 2011

Revised: October 19, 2011

s-SWCNTs with diameters in the 1.2–1.7 nm range. Nanotube bundling was prevented by forming nanofilaments of SWCNTs coated by an ordered P3HT layer prior to active layer deposition. This approach enabled us to measure and model the electrical and optical properties of the active layer for a wide range of nanotube loadings (up to 40 wt %). We find that nanotubes of specific diameter and chirality can act as efficient acceptors with internal quantum efficiency (IQE) of 26%, and that the open circuit voltage (V_{OC}), dark-saturation current (J_D), short-circuit current (J_{SC}), and series resistance (R_s) are strongly affected by the SWCNTs concentration with competing effects giving a maximum power conversion efficiency of 0.72% at 3 wt % nanotube loading.

P3HT/s-SWCNT nanofilaments used in the solar cells active layer were prepared starting from a solution of P3HT and high purity s-SWCNT (98% purity IsoNanotube-S powder from NanoIntegris, nominal diameter 1.2–1.7 nm). s-SWCNT were dissolved in 1,2-dichlorobenzene in concentration of 5 mg/mL and sonicated for 30 min, and a separate solution of P3HT (10 mg/mL, in 1,2-dichlorobenzene) was also prepared. The composition of the active layer was regulated by mixing together the two solutions in different proportions under stirring to achieve a 1,2-dichlorobenzene solution of P3HT/s-SWCNT with nanotube concentration of 0, 0.5, 1, 3, 5, 10, 20, 40 wt %. P3HT/s-SWCNT nanofilaments were prepared by progressively increasing the solvent polarity by the addition of cyclohexanone to favor P3HT aggregation onto the SWCNTs. Cyclohexanone (5–10 vol %) was quickly injected into the P3HT/s-SWCNT solution and aged overnight without stirring. The resulting solution, containing P3HT/s-SWCNT nanofilaments, showed no visible aggregation even after several days, and was used within 1–2 days of preparation to deposit the active layer.

For devices preparation, a PEDOT/PSS hole transporting layer was first deposited onto the ITO contact. Next, active layers consisting of both P3HT/s-SWCNT nanofilaments and, for comparison, a mixture of P3HT/s-SWCNT were spin-cast from solution using s-SWCNT weight fractions $x = 0, 1, 2, 3, 5, 10, 20$, and 40 wt %. Unless noted otherwise, active layers were not thermally annealed (when thermal annealing was performed, samples were heated at 140 °C for 10 min). A thin layer of BCP was used between the top Al metal electrode and the active layer to block the diffusion of excitons and holes to the metal electrode, as well as to reduce the damage of the active layer during the metal evaporation.

The wavelength-dependent quantum efficiency was measured using a lock-in amplifier with the sample under illumination from monochromatic light generated by a Xenon arc lamp coupled to a monochromator and chopped at 40 Hz. Transmittance and absorbance spectra of the device active layer were measured with a Cary 5000 UV–vis-NIR dual-beam spectrophotometer. Photoluminescence (PL) spectra were acquired at room temperature with a Cary Eclipse Fluorescence spectrometer with an excitation wavelength of 400 nm, and then normalized to the spectral response of the detector. Samples illumination was performed using a solar simulator lamp with 100 mW/cm² intensity and spectral distribution given by an AM1.5 global filter. A JEOL 2010 FEG analytical transmission electron microscope (TEM) operated at 200 kV was used for structural analysis. Device surface morphology was investigated using a Digital Instruments Dimension 3000 atomic force microscope (AFM) operated in tapping mode.

The device architecture used in this work is shown in Figure 1a. In the active layer, s-SWCNTs work as electron acceptors due to

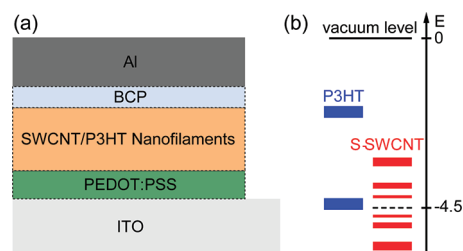


Figure 1. (a) Schematic of the solar cells used in this work (see details in the text). (b) Band alignment diagram for P3HT/s-SWCNTs interfaces used in this work. The positions of the SWCNT energy levels were determined based on the s-SWCNT diameter distribution and corresponding energy gap values from ref 14. The data used for SWCNT are derived from LDA density functional theory calculations, and slightly underestimate the nanotube electronic gaps and thus the band offsets, as discussed in ref 14. HOMO and LUMO band widths of 0.3 eV were used for P3HT.

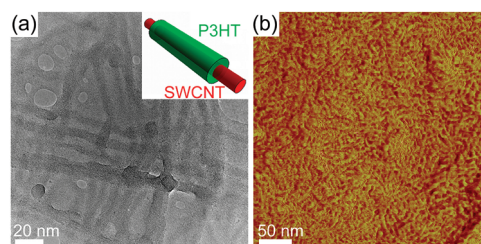


Figure 2. (a) Bright-field TEM image of a mixture of P3HT/s-SWCNTs nanofilament sample with SWCNT concentration $x = 3$ wt %. (Inset) Schematic image of a P3HT (green)/s-SWCNT (red) nanofilament prepared in this work. (b) AFM phase image of P3HT/s-SWCNT nanofilaments in a sample with SWCNT concentration $x = 3$ wt % showing the wormlike morphology of the active layer.

their higher electron affinity compared to P3HT. For the s-SWCNT used here, there are roughly 50 types of semiconducting SWCNT of different diameter and chirality (see Supporting Information), whose work functions are expected to be close to 4.5 eV based on the diameter size being greater than 1 nm.¹³ The n^{th} electronic transition energy (E_{nn}) specular to the Fermi level in the s-SWCNT was estimated using density functional theory data from Akai et al.¹⁴ Figure 1b shows the band alignment in the active layer with data for the polymer taken from Kanai et al.¹⁵ for the case of nonannealed P3HT deposited on ITO, and for s-SWCNT E_{nn} states up to $n = 3$.¹⁴

Figure 2 shows the active layer morphology resulting from the nanofilament preparation procedure described above. TEM (Figure 2a) and AFM (Figure 2b) images show formation of a film with wormlike morphology at the micrometer-length scale, composed of nanofilaments with average diameter of ~ 10 nm, significantly larger than the original 1–2 nm diameter of the isolated SWCNT. This suggests that a nanofilament structure is formed, constituted of up to a few SWCNTs coated by P3HT polymer layers (inset of Figure 2a), as further supported by photoabsorption measurements (see below). By contrast, TEM images of mixtures of P3HT/s-SWCNT spin-cast from solution show a typical amorphous morphology with SWCNT embedded in a P3HT matrix (not shown).

To assess the impact of the structural ordering in the P3HT/s-SWCNT nanofilaments, we next performed photoabsorption and

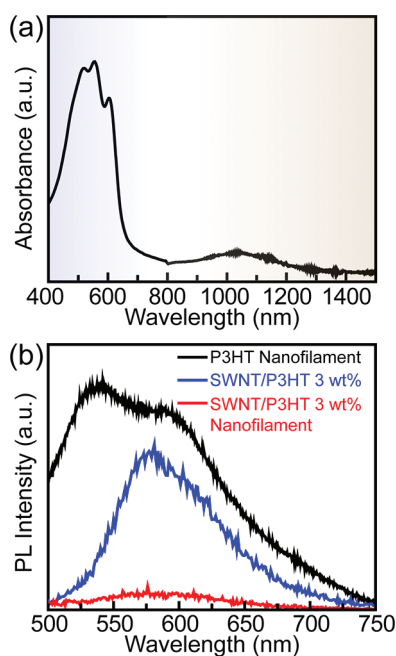


Figure 3. (a) Optical photoabsorption of a thin layer of P3HT/s-SWCNT nanofilaments with SWCNT concentration $x = 3$ wt %, showing contributions to the absorbance from P3HT in the visible and from SWCNTs in the infrared (shaded blue and brown, respectively). (b) PL intensity measurements for different P3HT/s-SWCNT morphologies. The nanofilament morphology (red curve) shows stronger quenching of the PL in the visible part of the spectrum compared to a simple mixture of P3HT and s-SWCNT (blue curve).

PL measurements on the device active layers. The photoabsorption spectrum of P3HT/s-SWCNT nanofilaments (Figure 3a) shows a strong absorption peak at 610 nm indicating a high degree of structural order in the polymer layer¹⁶ in support of our model of the nanofilament structure. Figure 3b compares PL spectra of three different thin film samples deposited on ITO: a film of pristine P3HT nanofilaments prepared with the method described above but in the absence of SWCNTs, a random s-SWCNT/P3HT mixture, and a P3HT/s-SWCNT nanofilament sample, both with s-SWCNT concentration of 3 wt %. The PL quenching of the P3HT/s-SWCNT nanofilaments is larger than in the case of the random P3HT/s-SWCNT mixture spin-cast from solution (Figure 3b), suggesting that well-ordered P3HT layers in the nanofilament configuration form an intimate contact with the s-SWCNTs and can improve the dissociation of excitons generated in the polymer.

Central to the understanding and modeling of the exciton and charge carrier dynamics in the nanofilament active layer is the study of the electrical and optical properties of fabricated devices, and we next investigated their dependence on SWCNT concentration. Figure 4a shows operating characteristics of nonannealed P3HT/s-SWCNT nanofilament devices at different nanotube concentrations (the results were obtained by averaging measurements from more than 20 devices for each nanotube concentration with a standard deviation of 4–5%); we report the complete set of results in Table 1, and the I - V curve for the device with highest efficiency in the Supporting Information. Both the open-circuit voltage and the short-circuit current density are seen to increase with nanotube loading at low SWCNT weight concentrations ($x < 3\%$), until a peak value of $V_{OC} = 1.04$ V

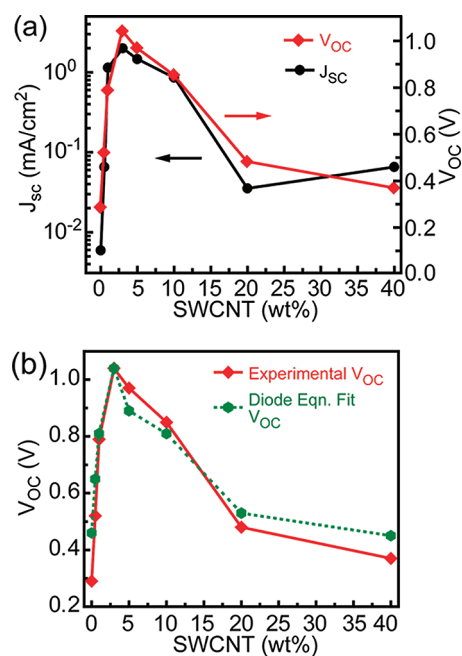


Figure 4. (a) Experimental values of the open-circuit voltage (red curve) and short-circuit current (black curve) as a function of the SWCNT weight fraction in the active layer for P3HT/s-SWCNT nanofilament based solar cells. The standard deviation on the currents and voltages is 4–5% based on measurements from more than 20 devices for each nanotube concentration. (b) Comparison of the experimental values of the open-circuit voltage (red curve) and a fit based on a biased diode eq 2 (green curve). For SWCNT concentrations $x > 1\%$ the dependence of V_{OC} on J_{SC} and J_D is well captured by the diode equation in a regime with significant carrier recombination.

Table 1. Electrical Properties of Devices with Different Nanotube Loadings^a

s-SWCNT concentration (wt %)	V_{OC} (V)	J_{SC} (mA/cm ²)	J_D (μA/cm ²)
0	0.29	5.99×10^{-3}	1.99
0.5	0.52	6.54×10^{-2}	0.57
1	0.79	1.14	0.43
3	1.04	1.99	0.01
5	0.97	1.46	0.11
10	0.85	0.86	0.32
20	0.48	3.53×10^{-2}	3.20
40	0.37	6.54×10^{-2}	21.10

^a Measured device characteristics at different SWCNT loadings for cells with s-SWCNT/P3HT nanofilaments in the active layer and prepared without thermal annealing. A large increase is seen in the dark saturation current above the optimal concentration $x = 3\%$, accompanied by a decrease of the open-circuit voltage and short-circuit current.

and $J_{SC} = 1.99$ mA/cm² is achieved at $x \approx 3$ wt %, a SWCNT concentration value three times larger than the previously reported optimal concentration for mixed metallic and semiconducting SWCNTs devices.⁴ Notably, for the best device with $x \approx 3$ wt % we measured an AM1.5 power conversion efficiency of 0.72%, which represents an increase by a factor of 15–20 over previously reported devices where both semiconducting and metallic SWCNTs were employed in combination with a polymer.^{3–6}

Table 2. Series Resistance of Devices with Different Active Layer Morphology^a

active layer morphology	series resistance (k Ω /cm ²)
no nanofilaments with thermal annealing	1.5×10^4
no nanofilaments no thermal annealing	1.9×10^3
with nanofilaments with thermal annealing	3.4×10^2
with nanofilaments no thermal annealing	32

^aThe heat treatment increases the series resistance by an order of magnitude both in the presence and in the absence of nanofilaments in the active layer. The series resistance decreases by three orders of magnitude by using P3HT/s-SWCNT nanofilaments without thermal annealing compared to the typical annealed film deposited from solution without SWCNTs passivation.

For the same SWCNT concentration (3 wt %), we also observe an increase in the J_{SC} by a factor of ~ 350 compared to devices where only P3HT was used in the active layer (see $x = 0$ entry in Table 1), a clear sign that at least a fraction of the s-SWCNTs form type-II heterojunctions and can effectively dissociate excitons in the active layer. The increase in V_{OC} and J_{SC} at small SWCNT concentrations ($x < 3$ wt %) can be attributed to the incipient formation of a continuous percolating network in the SWCNT phase that allows charge extraction out of the device, similar to the behavior observed in BHJ blends based on nanowires.¹⁷ At SWCNT fraction higher than 3 wt % both J_{SC} and V_{OC} decrease for increasing nanotube concentration, while J_D increases by over 3 orders of magnitude (see Table 1). We analyze here these effects by focusing on the decrease of the open circuit voltage for SWCNT concentrations above $x = 3$ wt %.

In the absence of s-SWCNT in the film and thus for an ITO/P3HT/Al device with intermediate blocking layers, the measured V_{OC} of 0.29 V (see $x = 0$ entry in Table 1) is in agreement with the metal–insulator–metal model⁴ with an interface loss of 0.1 eV, given a 0.4 eV difference in the work function of ITO and Al. When nanotubes are introduced and a percolation network is established, the picture changes dramatically, giving rise to an anomalously large V_{OC} . Despite a modest SWCNT-LUMO/P3HT-HOMO interface gap of $\Delta \approx 0.2$ – 0.3 eV inferred from the flat band diagram (Figure 1b), a large open-circuit voltage of 1.04 V is measured at $x = 3\%$. A similar effect ($V_{OC} = 0.75$ V) was observed by Kymakis et al. for P3OT/SWCNT devices in the presence of both metallic and semiconducting nanotubes and was attributed to a regime in which the value of the interface gap controls V_{OC} .^{4,18} Recent models set the interface gap as the upper limit for V_{OC} ,^{19,20} but the V_{OC} values observed here for s-SWCNT/P3HT are much larger than the interface gap and thus cannot be explained within such models, and we discuss here a possible explanation for this behavior.

The V_{OC} can be related to Δ , J_{SC} , and J_D by a diode equation²⁰

$$V_{OC} = \frac{nkT}{e} \log \left(\frac{J_{SC}}{J_D} \right) \quad (1)$$

where e is the electron charge, T is the absolute temperature, k is the Boltzmann constant, n is the diode ideality factor, and the dark current $J_D = J_0 e^{-\Delta/nkT}$ depends exponentially on the interface gap with a coefficient J_0 that can be interpreted as an elastic tunneling current and is related to the overlap of the frontier orbitals in the donor and the acceptor, and the density of states at the HOMO and LUMO levels.²⁰ In our devices, we observe a strong dependence of J_D on the SWCNT concentration that

increases by a factor of 2500 from $x = 3$ wt % to $x = 40$ wt % (see Table 1) despite a value for the interface gap Δ expected to be relatively insensitive to the SWCNT concentration. This suggests that J_D depends strongly on factors other than the interface gap Δ in our case, and we hypothesize that J_D and V_{OC} are regulated by carrier recombination mechanisms other than thermal generation of electron–hole pairs across the donor–acceptor interface, leading to corrections to eq 1.

Similar to our measurements, Kymakis et al. also observed an increase of the dark current by a factor of 10 when the SWCNT weight fraction was increased from 1 to 5 wt % and suggested that a longer conjugation length is achieved in the polymer-SWCNTs blend compared to the pristine polymer device, inducing an increased tunneling rate J_0 across the interface.⁴ This effect has recently been shown both theoretically and experimentally,²¹ but it can account only for a small part of the increase of J_D measured in our case (a factor of ~ 20 based on increase in J_0 calculated using data from ref 21 vs a factor of ~ 2500 measured when the nanotube concentration is increased from $x = 3$ wt % to $x = 40$ wt %). We note that an increase in the SWCNT concentration leads to a nanotube network that constitutes a larger part of the active layer, and multiple effects (e.g., the formation of a large number of nanotube–nanotube junctions and of confined polymer domains) modify the transport and the interface electronic and molecular structure in the blend, with an overall decrease of the carrier diffusion length confirmed by a drop in J_{SC} and by the corresponding large increase in J_D .

For SWCNT concentrations higher than $x = 1\%$, we found that the open circuit voltage can be related to the dark and short-circuit currents using a modified diode equation

$$V_{OC} = \frac{nkT}{e} \log \left(\frac{J_{SC}}{J_D} \right) + W \quad (2)$$

where $W = 0.76$ eV is a biasing constant used here to match the value of V_{OC} for $x = 3$ wt %, and we set $n = 2$ for a regime where carrier recombination is dominant.²⁰ With this choice, we find that for $x > 1$ wt % the dependence of V_{OC} on the SWCNT concentration through the values of J_{SC} and J_D can be well captured by the simple diode eq 2 (see Figure 4b). The excellent agreement between our data and eq 2 strongly supports our hypothesis that V_{OC} is regulated by carrier recombination processes with J_D that does not depend exponentially on the value of the interface gap Δ associated with the P3HT/s-SWCNT interface, that is too small here to account for the observed V_{OC} at intermediate concentrations. In general, modeling and understanding the origin of the V_{OC} is highly complex,²² and these aspects of P3HT/s-SWCNT blends deserve further investigation. For example, the physical origin of the correction W used here could be due space-charge effects, hot-carriers, parallel diodes, or their combination.

The transport properties and electrical device characteristics are further affected by the active layer morphology. As discussed above, the P3HT/s-SWCNT nanofilaments play a key role in improving transport in the device, as we further verify through measurement of the series resistance for devices with a range of nanotube loadings. The measured series resistances are summarized in Table 2 for devices with nanofilaments morphology and for devices prepared by spin-casting of a mixture of P3HT and s-SWCNT, both with and without thermal annealing. The series resistance decreased by 3 orders of magnitude in nanofilament devices without annealing compared to devices based on

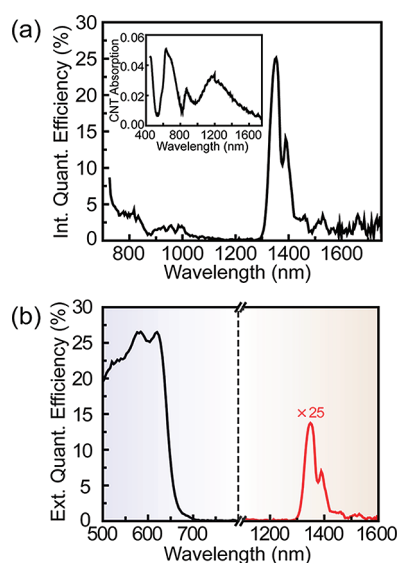


Figure 5. (a) Internal quantum efficiency of a device with s-SWCNT concentration $x = 3$ wt.%, shown here in the spectral range of 800–1600 nm (the main contribution to the IQE in the visible region corresponding to P3HT is not shown). A peak IQE of 26% is achieved for wavelengths in the range of 1300–1400 nm. The inset shows absorption in the active layer due to the SWCNTs, obtained by subtracting the P3HT spectrum from the spectrum of a P3HT-SWCNT sample, as explained in the Supporting Information. (b) External quantum efficiency showing features similar to the IQE (main contributions corresponding to P3HT and s-SWCNTs are shaded blue and brown, respectively). For clarity, the curve was multiplied by a factor of 25 in the near-infrared part of the spectrum.

a spin-cast mixture of P3HT and s-SWCNT with postdeposition annealing. This suggests that carrier transport is strongly dependent on the active layer morphology and is not controlled by ballistic conduction in the s-SWCNT phase but rather occurs in the diffusive regime in both the SWCNT and the P3HT phases. Thus, even in the presence of an acceptor with high carrier mobility like SWCNT carrier transport in the active layer seems to be a limiting factor for the device efficiency. In this perspective, the nanofilament morphology and its consequent enhancement of the molecular order in the P3HT phase and prevention of the SWCNT bundling play a critical role in improving the carrier transport. Moreover, thermal annealing degrades the transport properties in P3HT/s-SWCNT nanofilament devices as seen by the increase of the series resistance in annealed samples (Table 2), opposite to what observed in PCBM-based organic solar cells² where thermal annealing favors the formation of extended PCBM domains and enhances the carrier mobility in the P3HT and PCBM phases. This difference in the response to thermal treatments can be attributed to the presence of preformed nanofilaments in the active layer of our devices, where the P3HT and SWCNT morphology is efficient for charge transport and exciton dissociation, without need for further microstructure adjustments as in PCBM-based cells. On the contrary, thermal annealing can favor SWCNT aggregation and can modify the nanofilament structures, causing detrimental effects in the transport as observed here.

Combined studies of carrier transport and exciton formation, dissociation, and dynamics provide a comprehensive picture of the phenomena occurring in the P3HT/s-SWCNT active layer. To this end, we accompany our study of the electrical transport

with characterization of the optical absorption of the active layer as well as the quantum efficiency in the solar cell devices (Figure 5). Based on the Kataura plot²³ and the nominal SWCNTs diameter range, optical absorption from the s-SWCNTs in our sample is predicted to occur in two bands at approximately 800–1200 nm (S_{22} transitions) and 1400–2000 nm (S_{11} transitions). An optical absorption spectrum of the pristine s-SWCNTs in 1, 2-dichlorobenzene matches this prediction (see Supporting Information). Interestingly, the interaction with P3HT in the active layer significantly changes the SWCNT absorption. Subtracting the P3HT absorption spectrum from the absorption spectrum of the P3HT-SWCNT active layer (Figure 5a, inset), we find that both the S_{11} and S_{22} SWCNT absorption peaks were significantly blue shifted and now centered, respectively, at 1200 and 900 nm (vs 1600 and 1000 nm for the pristine SWCNTs). Such dramatic change can be explained either by the formation of a charge-transfer excited state or by a hybridization between the valence subbands in the SWCNT and the P3HT LUMO band, of particular relevance for the E_{11} levels of the nanotubes due to their near degeneracy with the P3HT LUMO band (as supported by the greater shift in the S_{11} transitions compared to the S_{22}).

The external and internal quantum efficiencies (EQE and IQE, respectively) were measured for optimal devices with nonannealed nanofilament morphology in the active layer at 3 wt % SWCNT (Figure 5a,b). The EQE shows a main contribution from P3HT for photon wavelength of 500–600 nm with an EQE around 25% indicative of effective dissociation of excitons generated within the polymer, which is in agreement with the PL quenching shown in Figure 3. The nanotubes also contribute to the photocurrent and carrier generation in the near-infrared, as confirmed by the analysis of the IQE and EQE in the spectral region at $\lambda > 800$ nm shown in Figure 5. All tested devices showed rather efficient photoconversion in the range 1300–1400 nm with a maximum IQE value of 26% at 1350 nm. On the basis of the absorption spectrum of the SWCNT in the active layer (Figure 5a, inset), we infer that the SWCNTs forming type-II heterojunctions favorable for charge separation have a diameter of 1.3–1.4 nm, that is, roughly the average diameter in the sample. SWCNTs falling in this diameter range and that are expected to contribute to the energy generation in the device (likely together with others of similar diameter) have chiral numbers (n,m) of (11,9), (12,7), (12,8), (13,6), (14,6), (15,4), (16,2), (16,3), (17,0) and (17,1) (see Supporting Information).

These results are in agreement with previous predictions that smaller diameter nanotubes improve the band offset and thus the charge separation,¹⁰ an effect in competition with the larger mobility and smaller exciton binding energy that would suggest the use of larger diameter tubes. The near absence of IQE signal from the region of $\lambda = 800$ –1100 nm also indicates that the S_{22} transitions do not contribute significantly to the photocurrent in our device in spite of the larger band offset. A similar effect has been observed in s-SWCNT/ C_{60} devices²⁴ and may be related to a different exciton decay dynamics for such excitations in the active layer.

In summary, P3HT/s-SWCNT solar cells with a range of nanotube concentrations and active layers morphologies were investigated. We found that a maximum device power conversion efficiency of 0.72% is achieved for nanofilament active layer morphology with $x = 3$ wt %. Key components for this improvement over previous SWCNT-based devices are the near absence of metallic tubes in the active layer and the use of nanofilaments of P3HT/s-SWCNT that induce a high degree of order in the P3HT phase and prevent SWCNT aggregation. We find a strong

dependence of the dark current and the open-circuit voltage on the SWCNT concentration, with a large value of V_{OC} of 1.04 V for the optimal SWCNT concentration of 3 wt %, in spite of a small and concentration-independent interface gap of ~ 0.3 eV. This suggests that charge and exciton transport and recombination strongly depend on the morphology and SWCNT weight fraction in the active layer. We show that P3HT/s-SWCNT heterojunctions can generate photocurrent from photons absorbed both in the P3HT and in the s-SWCNT and achieve an IQE of 26% in the near-infrared. These results motivate further investigation of P3HT/s-SWCNT solar cells to understand the distinct operational mechanisms from the PCBM-based counterpart.

■ ASSOCIATED CONTENT

S Supporting Information. List of materials used. Absorption spectrum of pristine SWCNTs. I – V curves. Experimental details of the quantum efficiency measurements. List of s-SWCNTs with diameter in the range 1.2–1.7 nm. This material is available free of charge via the Internet at <http://pubs.acs.org>.

■ AUTHOR INFORMATION

Corresponding Author

*E-mail: (S.G.) gradecak@mit.edu; (J.C.G.) jcg@mit.edu.

Author Contributions

^SThese authors contributed equally to this work.

■ ACKNOWLEDGMENT

This work was supported by Eni S.p.A. under the Eni-MIT Alliance Solar Frontiers Program. The authors acknowledge access to Shared Experimental Facilities provided by the MIT Center for Materials Science Engineering supported in part by MRSEC Program of National Science Foundation under award number DMR - 0213282.

■ REFERENCES

- (1) Zhu, H.; Wei, J.; Wang, K.; Wu, D. Applications of Carbon Materials in Photovoltaic Solar Cells. *Sol. Energy Mater. Sol. Cells* **2009**, *93*, 1461–1470.
- (2) Mayer, A. C.; Scully, S. R.; Hardin, B. E.; Rowell, M. W.; McGehee, M. D. Polymer-Based Solar Cells. *Mat. Today* **2007**, *10*, 28–33.
- (3) Kymakis, E.; Amaratunga, G. A. J. Single-Wall Carbon Nanotube/Conjugated Polymer Photovoltaic Devices. *Appl. Phys. Lett.* **2002**, *80*, 112–114.
- (4) Kymakis, E.; Amaratunga, G. A. J. In *Organic Photovoltaics*; Sun, S.-S., Sariciftci, N. S., Eds.; CRC Press: Boca Raton, FL, 2005.
- (5) Landi, B. J.; Raffaele, R. P.; Castro, S. L.; Bailey, S. G. *Prog. Photovoltaics* **2005**, *13*, 165–172.
- (6) Adikaari, A. A. D. T.; Dissanayake, D. M. N. M.; Silva, S. R. P. *IEEE J. Sel. Top. Quantum Electron.* **2010**, *16*, 1595–1606.
- (7) Holt, J. M.; Ferguson, A. J.; Kopidakis, N.; Larsen, B. A.; Bult, J.; Rumbles, G.; Blackburn, J. L. *Nano Lett.* **2010**, *10*, 4627–4633.
- (8) Kanai, Y.; Grossman, J. C. *Nano Lett.* **2008**, *8*, 908–912.
- (9) Bindl, D. J.; Safron, N. S.; Arnold, M. S. *ACS Nano* **2010**, *4*, 5657–5664.
- (10) Stranks, S. D.; Weisspfenning, C.; Parkinson, P.; Johnston, M. B.; Herz, L. H.; Nicholas, R. J. *Nano Lett.* **2011**, *11*, 66–72.
- (11) Capaz, R. B.; Spataru, C. D.; Ismail-Beigi, S.; Louie, S. G. *Phys. Status Solidi B* **2007**, *244* (11), 4016–4020.
- (12) Zhao, Y.; Liao, A.; Pop, E. *IEEE Electron. Device Lett.* **2009**, *30*, 1078–1080.
- (13) Barone, V.; Peralta, J. E.; Uddin, J.; Scuseria, G. U. *J. Chem. Phys.* **2006**, *124*, 2.

(14) Akai, Y.; Saito, S. *Physica E* **2005**, *29*, 555. These values are derived from LDA density functional theory calculations and thus underestimate the nanotube electronic gaps and band offsets. More accurate calculations using the GW method show that LDA underestimates the gap of tubes with diameter $d > 1$ nm only by $\sim 10\%$, so that for the present work the LDA predictions for the band gaps are accurate within a 10% error. For details, see Miyake, T.; Saito, S. *Phys. Rev. B* **2003**, *68*, 155424.

(15) Kanai, K.; Miyazaki, T.; Suzuki, H.; Inaba, M.; Ouchi, Y.; Seki, K. *Phys. Chem. Chem. Phys.* **2010**, *12*, 273–282.

(16) Brown, P. J.; Thomas, D. S.; Kohler, A.; Wilson, J. S.; Kim, J.-S.; Ramsdale, C. M.; Sirringhaus, H.; Friend, R. H. *Phys. Rev. B* **2003**, *67*, 064203.

(17) Ren, S.; Zhao, N.; Crawford, S. C.; Tambe, M.; Bulovic, V.; Gradecak, S. *Nano Lett.* **2011**, *11*, 408–413.

(18) Kymakis, E.; Alexandrou, I.; Amaratunga, G. A. J. *J. Appl. Phys.* **2003**, *93*, 1764.

(19) Giebinik, N. C.; Wiederrecht, G. P.; Wasielewski, M. R.; Forrest, S. R. *Phys. Rev. B* **2010**, *82*, 155305.

(20) Perez, M. D.; Borek, C.; Forrest, S. R.; Thompson, M. E. *J. Am. Chem. Soc.* **2009**, *131*, 9281–9286.

(21) Bernardi, M.; Giulianini, M.; Grossman, J. C. *ACS Nano* **2010**, *4*, 6599.

(22) Deibel, C.; Dyakonov, V. *Rep. Prog. Phys.* **2010**, *73*, 096401.

(23) Kataura, H.; Kumazawa, Y.; Maniwa, Y.; Umez, I.; Suzuki, S.; Ohtsuka, Y.; Achiba, Y. *Synth. Met.* **1999**, *103*, 2555–2558.

(24) Bindl, D. J.; Wu, M.-Y.; Prehn, F. C.; Arnold, M. S. *Nano Lett.* **2011**, *11*, 455–460.